

Extremely efficient terahertz high harmonic generation in graphene by hot Dirac fermions

Hafez, H. A.; Kovalev, S.; Deinert, J.-C.; Mics, Z.; Green, B.; Awari, N.; Chen, M.; Germanskiy, S.; Lehnert, U.; Teichert, J.; Wang, Z.; Tielrooij, K.-J.; Liu, Z.; Chen, Z.; Narita, A.; Müllen, K.; Bonn, M.; Gensch, M.; Turchinovich, D.;

Originally published:

September 2018

Nature 561(2018), 507-511

DOI: <https://doi.org/10.1038/s41586-018-0508-1>

Perma-Link to Publication Repository of HZDR:

<https://www.hzdr.de/publications/Publ-27847>

Release of the secondary publication
on the basis of the German Copyright Law § 38 Section 4.

1 **Extremely efficient terahertz high harmonics generation in graphene by hot Dirac
2 fermions**

3
4 Hassan A. Hafez^{1,2,3+}, Sergey Kovalev⁴⁺, Jan-Christoph Deinert⁴, Zoltan Mics², Bertram Green⁴,
5 Nilesh Awari^{4,5}, Min Chen⁴, Semyon Germanaskiy⁴, Ulf Lehnert⁴, Jochen Teichert⁴, Zhe Wang⁴, Klaas-
6 Jan Tielrooij⁶, Zhaoyang Liu², Zongping Chen², Akimitsu Narita², Klaus Müllen², Mischa Bonn²,
7 Michael Gensch⁴, and Dmitry Turchinovich^{1,2}

8
9 ¹Fakultät für Physik, Universität Duisburg-Essen, Lotharstraße 1, 47057 Duisburg, Germany

10 ²Max Planck Institute for Polymer Research, Ackermannweg 10, 55128 Mainz, Germany

11 ³Physics Department, Faculty of Science, Helwan University, 11792, Cairo, Egypt

12 ⁴Helmholtz-Zentrum Dresden-Rossendorf, Bautzner Landstraße 400, 01328 Dresden, Germany

13 ⁵University of Groningen, 9747 AG Groningen, The Netherlands

14 ⁶ICFO—Institut de Ciències Fotoniques, The Barcelona Institute of Science and Technology, Castelldefels,
15 Barcelona 08860, Spain

16
17 ⁺contributed equally to this work

18
19 Multiple optical harmonics generation – the multiplication of photon energy as a result of
20 nonlinear light-matter interaction, has become one of the key technologies in modern electronics
21 and optoelectronics. Owing to its unique electronic band structure featuring massless Dirac
22 fermions [1–3], graphene has been repeatedly predicted to possess particularly high efficiency of
23 optical harmonics generation in the technologically important terahertz (THz) frequency range [4–
24 6]. However, to date, numerous experiments have unfortunately failed to confirm these predictions
25 under technologically-relevant operation conditions. Here we report on the generation of THz
26 harmonics up to the seventh order in single-layer graphene at room temperature and under
27 ambient conditions, driven by THz fields on the order of only 10s of kV/cm, and with field
28 conversion efficiencies in excess of 10⁻³, 10⁻⁴, and 10⁻⁵ for the third, fifth, and seventh THz
29 harmonics, respectively. The key to highly efficient THz harmonics generation in graphene is the
30 collective thermal response of its background Dirac electrons to the driving THz fields. The
31 generated THz harmonics were observed directly in the time domain as electromagnetic field
32 oscillations at these newly synthesized frequencies. The effective THz nonlinear optical coefficients
33 of graphene $\chi^{(3)}_{\text{eff}} \approx 10^{-9} \text{ m}^2/\text{V}^2$, $\chi^{(5)}_{\text{eff}} \approx 10^{-22} \text{ m}^4/\text{V}^4$, and $\chi^{(7)}_{\text{eff}} \approx 10^{-38} \text{ m}^6/\text{V}^6$ substantially exceed the
34 respective nonlinear coefficients of typical solids by 7–18 orders of magnitude [7–9]. Our results, in
35 particular, provide a direct pathway to highly efficient THz frequency synthesis already within the
36 present generation of graphene electronics operating at the fundamental frequencies of only a few
37 100s of GHz.

38 A very strong demand exists in the field of modern ultrahigh-speed electronics for efficient active
39 functional materials supporting very high, terahertz (10^{12} Hz, THz), frequencies. Since the advent
40 of graphene, several theoretical proposals (see e.g. [4–6]) have predicted efficient THz frequency
41 multiplication or harmonics generation in single-layer graphene in realistic technologically-
42 relevant scenarios, which includes room temperature operation. Despite considerable efforts, the
43 experimental verification of these predictions has so far not been achieved. Bowlan et al. [10]
44 have recently demonstrated signatures of THz harmonics in a near-intrinsic epitaxial 45-layer

45 graphene sample, however only observable at a cryogenic temperature. The nonlinearity
46 mechanism in Ref. [10] critically relies on inter-band THz transitions in graphene, which at a room
47 temperature are essentially Pauli-blocked. Further, most recently, it was suggested that efficient
48 THz harmonics generation in graphene is unfeasible [11] due to the ultrafast relaxation of THz-
49 excited electrons and holes, prohibiting coherent electronic response to driving THz fields, which is
50 typically required for the generation of THz or optical harmonics in other solids [12,13].
51 Consequently, it was proposed to move away from the THz range to much higher infrared optical
52 frequencies, where Yoshikawa et al. [11] successfully demonstrated the generation of multiple
53 optical harmonics in single-layer graphene under intense optical excitation with peak electric field
54 strengths reaching 10s of MV/cm.

55 Here we show that the THz high harmonics generation in single-layer graphene under realistic
56 technological conditions is, in fact, an extremely efficient process, and that the THz nonlinearity of
57 this atomically-thin material greatly surpasses that of other solids. We demonstrate THz harmonics
58 generation up to the 7th order in single-layer graphene at room temperature and under ambient
59 conditions, using THz electric fields as weak as only 10s of kV/cm, which is about three orders of
60 magnitude lower (corresponding to one million times smaller peak powers) than that required for
61 the observation of infrared-driven nonlinearity [11].

62 Previous experiments on the generation of optical harmonics in graphene critically relied on
63 interband transitions in graphene in strong applied fields [10,11]. Here we show that the key to
64 highly efficient THz harmonics generation in graphene is the introduction of the *free background*
65 electron population, responding *collectively* to the driving THz field. These free background Dirac
66 electrons, which can be easily introduced by the substrate or atmospheric doping, or by electronic
67 gating, serve as an extremely efficient, yet highly nonlinear, intermediary energy reservoir: they
68 facilitate and also strongly modulate the energy transfer between the THz field and graphene via a
69 *nonlinear intraband conductivity* mechanism. Our experimental observations are fully reproduced
70 by a model describing such energy transfer dynamics and the concurrent THz electromagnetic
71 response of graphene.

72 Our sample is a typical chemical vapor deposition (CVD)-grown monolayer graphene deposited on
73 a fused SiO₂ substrate (see Ref. [14] and references therein). Basic characterization of the sample
74 yielded a background free carrier concentration of $N_c = 2.1 \times 10^{12} \text{ cm}^{-2}$ and Fermi level of $E_F = 170$
75 meV at room temperature (see **Methods** and **Extended Data** Fig. 11).

76 Our experiment, schematically represented in Fig. 1(a), was specifically designed for the
77 observation of the THz harmonics in graphene in the time domain (see **Methods** and **Extended**
78 **Data** Fig. 1). It was enabled by the use of TELBE - a novel superconducting radio-frequency
79 accelerator-based superradiant THz source [15]. Our measurements were performed at a
80 repetition rate of 100 kHz, and with linearly polarized THz electric fields incident normally onto
81 graphene. Narrow-band, multi-cycle quasi-monochromatic THz radiation pulses from TELBE (see
82 **Extended Data** Fig. 2) with controllable peak field strength in the range of $E_f = 12 - 85 \text{ kV/cm}$ and
83 FWHM bandwidth of below 70 GHz were transmitted through the single-layer graphene deposited
84 on a SiO₂ substrate, and were detected in the time-domain as the THz light-wave oscillations (see
85 **Methods** and **Extended Data** Fig. 1). The THz transmission through a nominally identical bare SiO₂
86 substrate served as a reference, which exhibited no sign of THz nonlinearity. The cut-off frequency

87 of our THz detector was 2.4 THz. All the measurements were carried out at room temperature.

88 In Fig. 1(b,c) we show the typical results of our experiments. In Fig. 1(b) we show the amplitude
89 spectra of the pump THz wave with a fundamental frequency of $f = 0.3$ THz and a peak electric
90 field strength of $E_f = 85$ kV/cm, transmitted only through the bare SiO₂ substrate (red line), and
91 through the single-layer graphene on the SiO₂ substrate (blue line). Multiple THz harmonics up to
92 the 7th order are clearly visible in the spectrum of the THz signal after interaction with graphene,
93 with a pump-to-harmonic field conversion efficiency in excess of 10^{-3} , 10^{-4} , and 10^{-5} for the third,
94 fifth, and seventh THz harmonics, respectively. Such significant nonlinear conversion efficiencies,
95 especially observed at THz frequencies, are quite remarkable, given that the electromagnetic
96 interaction occurs here within just one single atomic layer. In Fig. 1(c) we demonstrate the
97 measured THz harmonics directly in the time domain. Fig. 1(d) shows the results of the calculation
98 based on the thermodynamic model of THz nonlinearity in graphene [14], using the experimental
99 THz pump wave at fundamental frequency $f = 0.3$ THz as an input. We note that the calculations in
100 Fig. 1(d) capture well all the key experimental features in Fig. 1(c), including the peak field strength
101 in the generated harmonics, as well as the temporal shortening of the harmonic pulses with the
102 increase in harmonic order. The essentials of our parameter-free model [14] are explained below,
103 while the specific calculation details are provided in [Methods](#).

104 The underlying physical mechanism of THz harmonics generation in graphene is the creation of
105 nonlinear electrical currents resulting from the strongly nonlinear *intraband* THz conductivity of
106 graphene background electrons. In electronic thermal equilibrium the intraband conductivity of
107 graphene σ is determined by the concentration N_c and the temperature T_e of its background
108 electronic population. For the intraband THz excitation of graphene $N_c = \text{const}$, and the
109 conductivity σ is thus governed by the electronic temperature T_e . If graphene is sufficiently doped,
110 so that $|E_F| > k_B T_e$, the rise in the electronic temperature leads to a reduction of
111 conductivity [14,16–18] (here k_B is the Boltzmann constant). The application of THz electric field E
112 to graphene leads to generation of a THz current $j = \sigma E$, and hence to deposition of energy into the
113 electronic population (the power absorption coefficient of a material is directly proportional to its
114 conductivity). One of the remarkable features of Dirac electrons in graphene is their ability to
115 internally thermalize, i.e. exchange their kinetic energy and establish a common electronic
116 temperature within the entire background electron population, on an ultrafast timescale below
117 100 femtoseconds [14,19–24], which is quasi-instantaneous as compared to the ~picosecond
118 period of the THz field oscillation. Therefore, via such an ultrafast internal electronic
119 thermalization, the excess energy deposited into graphene background electrons by the THz
120 current is quasi-instantaneously converted into electronic heat – the collective kinetic energy of
121 the *entire* background electron population, leading to a *rise* in the electronic temperature T_e and
122 to a concomitant *decrease* of the intraband conductivity σ . As a result of these interdependencies,
123 the THz conductivity of graphene depends strongly nonlinearly on the driving THz
124 field [14,17,25,26]: the stronger the field, the smaller the conductivity becomes.

125 The subsequent energy relaxation (i.e. cooling) of the hot electron population in graphene occurs
126 via phonon emission on a timescale of a few picoseconds (see e.g. [20,25]), i.e. with THz rate (see
127 [Methods](#)). This phonon emission completes the energy conversion process in the THz excitation of
128 graphene, in which the background population of Dirac electrons serves as a nonlinear
129 intermediary in the transfer of energy from the absorbed THz field to the lattice of graphene.

130 The processes of heating and cooling of background Dirac electron population, leading to the
131 reduction and recovery of the intraband THz conductivity in graphene, respectively, are
132 schematically shown in Fig. 2(a). Here $N(E) = D(E)f_{\text{FD}}(E,T)$ is the energy-dependent population
133 density function for graphene background electrons, a product of the density of states D and the
134 Fermi-Dirac distribution f_{FD} . Now we arrive at a situation where the THz conductivity of graphene
135 is not only nonlinear with the driving THz field (as facilitated by the direct conversion of absorbed
136 THz energy into electronic heat), but also exhibits THz-rate recovery dynamics provided by the
137 electron cooling rate (transfer of electronic heat to the lattice). The double interplay of quasi-
138 instantaneous electron heating and THz-rate electron cooling in THz-driven graphene leads to
139 highly nonlinear *temporal modulation* of the THz absorption in graphene, and hence of the THz
140 conductivity, as illustrated in the calculations shown in Figs. 2(b,c,d) (see [Methods](#) for details).
141 Consequently, a nonlinear current modulated by nonlinear time-dependent conductivity, is
142 generated in graphene in response to the driving THz field $E(t)$. In case of a monochromatic THz
143 driving field $E_f(t)$ oscillating at a frequency f , the resulting nonlinear current in graphene, given its
144 centrosymmetry, will contain contributions at odd-order harmonics $f, 3f, 5f, 7f, \dots$, thus leading to
145 electromagnetic re-emission at these harmonic frequencies, as illustrated schematically in Fig.
146 1(a), and resulting in the appearance of these harmonics in the spectrum of the transmitted THz
147 signal. We note that in a centrosymmetric medium the even-order harmonics cancel out, and thus
148 cannot be generated [7]. Using the above thermodynamic model [14] the nonlinear propagation
149 of THz signals through graphene can be readily calculated, only using experimentally determined
150 parameters as input: the incident THz waveform at the fundamental frequency f ; the conductivity
151 parameters of the graphene sample measured in the linear regime in full thermal equilibrium at T
152 = 300 K; the quasi-instantaneous electron heating (see discussion above and Refs. [19–24]), and
153 picosecond-timescale cooling via phonon emission as measured in Ref. [20]. We also note that no
154 adjustable parameters are used in our model (see [Methods](#)).
155 Now we determine the harmonic generation efficiency and estimate the effective THz nonlinear
156 optical susceptibility of graphene from the analysis of experimentally-measured time-domain THz
157 signals, such as those shown in Fig. 1(c). In Fig. 3(a), we show the dependency of the amplitude of
158 the generated harmonics fields on that of the driving field. Here, in order to increase the dynamic
159 range in the characterization of the 3rd and 5th harmonics generation processes, our THz detection
160 scheme was optimized to detect the harmonic signal only in the spectral window around 2 THz,
161 whereas the driving fundamental frequency f of the THz source was varied as follows: $f = 0.68$ THz
162 was used to generate the 3rd harmonic at $3f = 2.04$ THz, and $f = 0.37$ THz was used to generate the
163 5th harmonic at $5f = 1.85$ THz. For the characterization of the 7th harmonic generation, the pump
164 field had the central frequency $f = 0.3$ THz, leading to the harmonic signal at $7f = 2.1$ THz, as shown
165 in Fig. 1(b,c). Depending on the order of the generated harmonic, the peak harmonic field strength
166 was in the range of 3 – 111 V/cm, whereas the pumping field strength was varying in the range of
167 12 – 85 kV/cm. The efficiency parameters of the THz harmonics generation in this work are
168 summarized in Table 1.
169

Generated harmonic order m	Range of pump field strength E_f , kV/cm	Range of harmonic field strength E_{mf} , V/cm	Max. field conversion efficiency E_{mf}/E_f	Effective nonlinear coefficient $\chi^{(m)}_{eff}$
3	12 - 61	3 – 111	2×10^{-3}	$\sim 10^{-9} \text{ m}^2/\text{V}^2$
5	17 - 60	0.4 – 15	2.5×10^{-4}	$\sim 10^{-22} \text{ m}^4/\text{V}^4$
7	38 - 85	1 – 7	8×10^{-5}	$\sim 10^{-38} \text{ m}^6/\text{V}^6$

Table 1. *Harmonic generation efficiencies and nonlinear coefficients of graphene.* Pump and harmonic peak electric field strength ranges, maximum field conversion efficiency, and the THz nonlinear coefficients of graphene of 3rd, 5th and 7th orders, established in the small-signal nonlinearity regime.

In the same Fig. 3(a), as black solid lines, we present the results of the calculated pump-to-harmonic conversion efficiencies [14], using the parameter-free thermodynamic model as explained above. The agreement between the experimental data and the parameter-free calculation is quantitative. The pump-to-harmonics generation efficiency, shown in Fig. 3(a), saturates with the pump field increase, as caused by the dissipative nature of the interaction between the THz field and the graphene electrons. In Fig. 2(c,d) we show the calculated temporal evolution of the THz field-induced electronic heat $\Delta Q(t)$ and the instantaneous THz power absorbance $A(t)$ of our graphene sample, driven by the THz field at the fundamental frequency $f = 0.3 \text{ THz}$ shown in Fig 2(b), and with the field strength at the lower and upper limits of our experiment: 10 kV/cm and 85 kV/cm, respectively. At the weaker driving field of 10 kV/cm, the evolution of both $\Delta Q(t)$ and $A(t)$ is very small. Here, the nonlinear interaction conditions between the THz field and graphene remain approximately constant over the entire interaction period, thus manifesting the small-signal nonlinearity regime. On the other hand, as the driving THz field increases by about an order of magnitude to 85 kV/cm, the effect of the THz field on the electronic system of graphene becomes dramatic. At the peak of the interaction, the electronic heat $\Delta Q(t)$ peaks at $0.33 \mu\text{J}/\text{cm}^2$, leading to a reduction of the THz power absorbance of graphene by approximately 25%. Such a significant absorption saturation naturally limits the energy transfer rate from the driving THz field to the electronic system, subsequently leading to the observed saturable behavior of THz nonlinearity in graphene. The drastic difference between the THz-graphene interaction conditions for the cases of $E_f = 10 \text{ kV/cm}$ and $E_f = 85 \text{ kV/cm}$ in Fig. 2(c,d) illustrates the extremely nonlinear nature of the thermodynamic response of the Dirac electrons in graphene to the THz fields.

Importantly, at lower driving fields below approximately 20 kV/cm, both the data and the calculation of harmonics generation efficiency in Fig. 3(a) reduce to the phenomenological power-law dependencies $E_{mf} \propto E_f^m$, where m is the harmonic order (see dashed lines in Fig. 3(a)), manifesting the small-signal nonlinearity regime. In this regime the nonlinear conversion can be described within the framework of effective odd-order nonlinear optical coefficients $\chi^{(m)}_{eff}$, precisely as expected for the nonlinear response in a centrosymmetric medium. From the purely power-law fits to the field conversion efficiencies (dashed lines in Fig. 3), we determine the effective THz third-, fifth-, and seventh-order nonlinear coefficients of graphene as $\chi^{(3)}_{eff} \approx 10^{-9} \text{ m}^2/\text{V}^2$, $\chi^{(5)}_{eff} \approx 10^{-22} \text{ m}^4/\text{V}^4$, and $\chi^{(7)}_{eff} \approx 10^{-38} \text{ m}^6/\text{V}^6$, respectively (see **Methods** for details). These

values of THz nonlinear optical coefficients of graphene, determined by us at room temperature and under ambient conditions in a conventional CVD-grown single-layer graphene, exceed the corresponding nonlinearities of a typical solid by 7-18 orders of magnitude [7–9]. The third-order nonlinearity, obtained in this work, exceeds the corresponding values measured in single-layer graphene in the optical spectral range by 6-10 orders of magnitude [27–29] (we note, however, that the theoretical prediction of stronger optical-range response exists in the literature [30]); and the value reported in the infrared for the 50-layer graphene sample under cryogenic conditions and in strong magnetic field by at least one order of magnitude [31]. The fifth- and seventh order THz nonlinear coefficients of graphene have not been previously reported in the literature, to the best of our knowledge.

We note here that the thermodynamic model of graphene conductivity does not contain any *a-priori* defined effective nonlinear-optical coefficients of graphene, but rather describes the temporal evolution of the THz field-induced electronic heat and, hence, the instantaneous conductivity of graphene during its interaction with the incident THz electromagnetic wave of arbitrary shape. A very good agreement between our parameter-free calculation and the entirety of our data lends credence to our interpretation of the nature of the observed THz harmonics generation in graphene.

We estimate the limits of applicability of the purely thermodynamic picture of nonlinear THz response in doped graphene as the onset of coherent Bloch oscillations (see e.g. [13]), which in graphene will occur at a pump field strength of the order of 1-10 MV/cm (see [Methods](#)). Now we illustrate the potential for higher-order THz harmonics generation in graphene using the thermodynamic mechanism, for some typical experimental and technological scenarios. Employing the same material parameters of the graphene as used in this work, we apply a model quasi-monochromatic waveform at fundamental $f = 0.68$ THz with varying peak field strengths in the range 100 V/cm - 1 MV/cm. This range comprises the linear regime of \sim kV/cm THz fields, the regime of typical high-speed transistor channel fields of \sim 100 kV/cm [32], and extends to the TELBE operation regime under projected design parameters of 1 MV/cm [15]. In Fig. 3(b) we show the corresponding calculated amplitude spectra of the transmitted THz waveform as a function of the peak electric field strength of the incident fundamental wave. As the driving electric field strength increases, higher-order harmonics keep appearing in the spectrum, with the 13-th harmonic falling within the 10^6 dynamic range with respect to the transmitted fundamental, at the field strength of the driving signal of 1 MV/cm.

The very high THz nonlinear coefficients of graphene, measured in this work, suggest straightforward applications in ultrahigh-frequency (opto-)electronics. The driving electric field on the order of 10s of kV/cm, such as used here, is about one order of magnitude smaller than the typical channel field in ultra-high speed transistors [32]. Therefore, our results provide the direct pathway way to purely electronic THz frequency synthesis already within the present generation of graphene transistors operating at few-100s GHz fundamental frequencies [32]. Further, the observed nonlinear THz response of a single layer graphene can be made scalable, for example, by creating stratified structures with graphene-coated interfaces, or graphene-loaded waveguides or cavities. We finally note that our results on efficient THz harmonic generation in graphene by hot Dirac fermions can be potentially generalized to other representatives of the novel class of Dirac materials, such as topological insulators, or Weyl and Dirac semimetals [33].

254

255 **References**

- 257 1. K. S. Novoselov, A. K. Geim, S. V Morozov, D. Jiang, M. I. Katsnelson, I. V Grigorieva, S. V
258 Dubonos, and A. A. Firsov, "Two-dimensional gas of massless Dirac fermions in
259 graphene," *Nature* **438**, 197–200 (2005).
- 260 2. A. H. Castro Neto, F. Guinea, N. M. R. Peres, K. S. Novoselov, and A. K. Geim, "The
261 electronic properties of graphene," *Rev. Mod. Phys.* **81**, 109–162 (2009).
- 262 3. S. Das Sarma, S. Adam, E. H. Hwang, and E. Rossi, "Electronic transport in two-
263 dimensional graphene," *Rev. Mod. Phys.* **83**, 407–470 (2011).
- 264 4. S. A. Mikhailov, "Non-linear graphene optics for terahertz applications," *Microelectronics
265 J.* **40**, 712–715 (2009).
- 266 5. I. Al-Naib, J. E. Sipe, and M. M. Dignam, "High harmonic generation in undoped graphene :
267 Interplay of inter- and intraband dynamics," *Phys. Rev. B* **90**, 245423 (2014).
- 268 6. I. Al-Naib, M. Poschmann, and M. M. Dignam, "Optimizing third-harmonic generation at
269 terahertz frequencies in graphene," *Phys. Rev. B* **91**, 205407 (2015).
- 270 7. R. W. Boyd, *Nonlinear Optics*, 3rd ed. (Academic Press, 2008).
- 271 8. A. S. Reyna and C. B. de Araújo, "High-order optical nonlinearities in plasmonic
272 nanocomposites—a review," *Adv. Opt. Photonics* **9**, 720 (2017).
- 273 9. O. Reshef, E. Giese, M. Zahirul Alam, I. De Leon, J. Upham, and R. W. Boyd, "Beyond the
274 perturbative description of the nonlinear optical response of low-index materials," *Opt.
275 Lett.* **42**, 3225 (2017).
- 276 10. P. Bowlan, E. Martinez-Moreno, K. Reimann, T. Elsaesser, and M. Woerner, "Ultrafast
277 terahertz response of multilayer graphene in the nonperturbative regime," *Phys. Rev. B*
278 **89**, 41408 (2014).
- 279 11. N. Yoshikawa, T. Tamaya, and K. Tanaka, "High-harmonic generation in graphene
280 enhanced by elliptically polarized light excitation," *Science* **356**, 736–738 (2017).
- 281 12. B. Zaks, R. B. Liu, and M. S. Sherwin, "Experimental observation of electron-hole
282 recollisions," *Nature* **483**, 580–583 (2012).
- 283 13. O. Schubert, M. Hohenleutner, F. Langer, B. Urbanek, C. Lange, U. Huttner, D. Golde, T.
284 Meier, M. Kira, S. W. Koch, and R. Huber, "Sub-cycle control of terahertz high-harmonic
285 generation by dynamical Bloch oscillations," *Nat. Photonics* **8**, 119–123 (2014).
- 286 14. Z. Mics, K.-J. Tielrooij, K. Parvez, S. A. Jensen, I. Ivanov, X. Feng, K. Müllen, M. Bonn, and D.
287 Turchinovich, "Thermodynamic picture of ultrafast charge transport in graphene," *Nat.
288 Commun.* **6**, 7655 (2015).
- 289 15. B. Green, S. Kovalev, V. Asgekar, G. Geloni, U. Lehnert, T. Golz, M. Kuntzsch, C. Bauer, J.
290 Hauser, J. Voigtländer, B. Wustmann, I. Koesterke, M. Schwarz, M. Freitag, A. Arnold, J.
291 Teichert, M. Justus, W. Seidel, C. Ilgner, N. Awari, D. Nicoletti, S. Kaiser, Y. Laplace, S.
292 Rajasekaran, L. Zhang, S. Winnerl, H. Schneider, G. Schay, I. Lorincz, A. A. Rauscher, I.
293 Radu, S. Mährlein, T. H. Kim, J. S. Lee, T. Kampfrath, S. Wall, J. Heberle, A. Malnasi-
294 Csizmadia, A. Steiger, A. S. Müller, M. Helm, U. Schramm, T. Cowan, P. Michel, A. Cavalleri,
295 A. S. Fisher, N. Stojanovic, and M. Gensch, "High-Field High-Repetition-Rate Sources for
296 the Coherent THz Control of Matter," *Sci. Rep.* **6**, 22256 (2016).

- 297 16. S. Winnerl, M. Mittendorff, J. C. König-Otto, H. Schneider, M. Helm, T. Winzer, A. Knorr,
298 and E. Malic, "Ultrafast Processes in Graphene: From Fundamental Manybody
299 Interactions to Device Applications," *Ann. Phys.* **529**, 1700022 (2017).
- 300 17. M. M. Jadidi, J. C. König-Otto, S. Winnerl, A. B. Sushkov, H. D. Drew, T. E. Murphy, and M.
301 Mittendorff, "Nonlinear Terahertz Absorption of Graphene Plasmons," *Nano Lett.* **16**,
302 2734–2738 (2016).
- 303 18. H. A. Hafez, I. Al-Naib, M. M. Dignam, Y. Sekine, K. Oguri, F. Blanchard, D. G. Cooke, S.
304 Tanaka, F. Komori, H. Hibino, and T. Ozaki, "Nonlinear terahertz field-induced carrier
305 dynamics in photoexcited epitaxial monolayer graphene," *Phys. Rev. B* **91**, 35422
306 (2015).
- 307 19. M. Breusing, S. Kuehn, T. Winzer, E. Malić, F. Milde, N. Severin, J. P. Rabe, C. Ropers, A.
308 Knorr, and T. Elsaesser, "Ultrafast nonequilibrium carrier dynamics in a single graphene
309 layer," *Phys. Rev. B* **83**, 153410 (2011).
- 310 20. I. Gierz, J. C. Petersen, M. Mitrano, C. Cacho, I. C. E. Turcu, E. Springate, A. Stöhr, A. Köhler,
311 U. Starke, and A. Cavalleri, "Snapshots of non-equilibrium Dirac carrier distributions in
312 graphene," *Nat. Mater.* **12**, 1119–1124 (2013).
- 313 21. I. Gierz, F. Calegari, S. Aeschlimann, M. Chávez Cervantes, C. Cacho, R. T. Chapman, E.
314 Springate, S. Link, U. Starke, C. R. Ast, and A. Cavalleri, "Tracking primary thermalization
315 events in graphene with photoemission at extreme time scales," *Phys. Rev. Lett.* **115**,
316 86803 (2015).
- 317 22. T. Winzer and E. Malić, "Impact of Auger processes on carrier dynamics in graphene,"
318 *Phys. Rev. B* **85**, 241404 (2012).
- 319 23. J. C. W. Song, K. J. Tielrooij, F. H. L. Koppens, and L. S. Levitov, "Photoexcited carrier
320 dynamics and impact-excitation cascade in graphene," *Phys. Rev. B* **87**, 155429 (2013).
- 321 24. A. Tomadin, D. Brida, G. Cerullo, A. C. Ferrari, and M. Polini, "Nonequilibrium dynamics of
322 photoexcited electrons in graphene: Collinear scattering, Auger processes, and the
323 impact of screening," *Phys. Rev. B* **88**, 35430 (2013).
- 324 25. S. Winnerl, M. Orlita, P. Plochocka, P. Kossacki, M. Potemski, T. Winzer, E. Malic, A. Knorr,
325 M. Sprinkle, C. Berger, W. A. de Heer, H. Schneider, and M. Helm, "Carrier relaxation in
326 epitaxial graphene photoexcited near the Dirac point," *Phys. Rev. Lett.* **107**, 237401
327 (2011).
- 328 26. H. Y. Hwang, N. C. Brandt, H. Farhat, A. L. Hsu, J. Kong, and K. A. Nelson, "Nonlinear THz
329 conductivity dynamics in p-type CVD-grown graphene," *J. Phys. Chem. B* **117**, 15819–
330 15824 (2013).
- 331 27. E. Hendry, P. J. Hale, J. Moger, A. K. Savchenko, and S. A. Mikhailov, "Coherent nonlinear
332 optical response of graphene," *Phys. Rev. Lett.* **105**, 97401 (2010).
- 333 28. S. Hong, J. I. Dadap, N. Petrone, P. Yeh, J. Hone, and R. M. Osgood, "Optical third-harmonic
334 generation in graphene," *Phys. Rev. X* **3**, 21014 (2013).
- 335 29. N. Kumar, J. Kumar, C. Gerstenkorn, R. Wang, H. Chiu, A. L. Smirl, and H. Zhao, "Third
336 harmonic generation in graphene and few-layer graphite films," *Phys. Rev. B* **87**, 121406
337 (2013).
- 338 30. J. L. Cheng, N. Vermeulen, and J. E. Sipe, "Third-order nonlinearity of graphene: Effects of
339 phenomenological relaxation and finite temperature," *Phys. Rev. B* **91**, 235320 (2015).
- 340 31. J. C. König-Otto, Y. Wang, A. Belyanin, C. Berger, W. A. De Heer, M. Orlita, A. Pashkin, H.
341 Schneider, M. Helm, and S. Winnerl, "Four-Wave Mixing in Landau-Quantized Graphene,"
342 *Nano Lett.* **17**, 2184–2188 (2017).

- 343 32. F. Schwierz, "Graphene transistors: status, prospects, and problems," Proc. IEEE **101**,
344 1567–1584 (2013).
- 345 33. T. O. Wehling, A. M. Black-Schaffer, and A. V. Balatsky, "Dirac materials," Adv. Phys. **63**, 1–
346 76 (2014).

347

348 **Acknowledgments:**

349 D.T. acknowledges the financial support from the Deutsche Forschungsgemeinschaft (SFB 1242
350 "Non-Equilibrium Dynamics of Condensed Matter in the Time Domain", TP B08), European
351 Commission (EU Career Integration Grant EU CIG 334324 LIGHTER), and from the Max Planck
352 Society. M.G. and B.G. acknowledge support from the European Cluster of Advanced Laser Light
353 Sources (EUCALL) project which has received funding from the European Union's Horizon 2020
354 research and innovation program under grant agreement No 654220. K.J.T. acknowledges support
355 through the Mineco Young Investigator Grant (FIS2014-59639-JIN). J.T. and U.L. acknowledge
356 support from the EuCARD-2 project, which has received funding from the European Commission
357 under grant agreement No 312453. We are grateful to Prof. Jesper Lægsgaard, Keno Kreuer,
358 Eduard Unger, Wentao Zhang, Thales V.A.G. de Oliveira, and Dr. Martin Mittendorff for fruitful
359 discussions. We thank the ELBE team for the operation of TELBE facility.

360

361 **Author contributions:**

362 D.T. and M.G. conceived and supervised the project. H.A.H., S.K., J.C.D., Z.M., B.G., N.A., M.C., S.G.,
363 Z.W., D.T. and M.G. performed the nonlinear THz spectroscopy measurements and evaluated the
364 experimental data. H.A.H. and D.T. performed the modeling, with contributions from Z.M. and
365 K.J.T.. D.T., M.G. and M.B. interpreted the results, with contributions from all co-authors. Z.L.,
366 Z.C., A.N. and K.M. manufactured the samples. H.A.H. and D.T. characterized the linear THz
367 properties of the graphene / fused silica samples. U.L. and J.T. provided for the special mode of
368 high bunch charge operation of TELBE using the novel SRF photoinjector that enabled the
369 observation of the 7th harmonic. M.B. initiated and supported the THz studies on graphene at
370 MPI-P. D.T. and M.G. wrote the manuscript, with contributions from M.B., K.J.T., S.K. and H.A.H.
371 All co-authors discussed the results and commented on the manuscript.

372

373 **Author Information statement**

374 The authors declare no competing financial interests. The correspondence, the inquiries regarding
375 reprints and permissions, and requests for materials should be addressed to D.T.
376 (dmitry.turchinovich@uni-due.de) and M.G. (m.gensch@hzdr.de).

377

378 **Data and computer codes availability statement**

379 The datasets generated during and/or analyzed during the current study, as well as the
380 corresponding computer codes, are available from the corresponding authors on reasonable
381 request.

382

383

384

385 **Main figure legends**

386 **Fig. 1.** Schematic of the THz high harmonics generation experiment and the main results. (a)
 387 Schematic of the experiment: quasi-monochromatic, linearly polarized THz pump wave from the
 388 TELBE source is incident onto a graphene sample, single-layer CVD-grown graphene deposited on
 389 the SiO₂ substrate. Graphene had a Fermi level $E_F = 170$ meV, free carrier density $N_c = 2.1 \times 10^{12}$ cm⁻², and electron momentum scattering time $\tau = 47$ fs (all parameters correspond to full thermal
 390 equilibrium at 300K). The peak electric field strength of the pump THz signal was controlled in the
 391 range of 12 - 85 kV/cm, and the central frequency was varied in the range of 0.3 – 0.68 THz. The
 392 incident THz field drives the nonlinear current in graphene, leading to the re-emission at higher
 393 odd-order harmonics that appear in the spectrum of the transmitted THz signal. The THz fields are
 394 detected in the time domain directly as oscillations of electric field, using free-space electro-optic
 395 sampling with the cut-off frequency at 2.4 THz. All the experiments are carried out at room
 396 temperature and under ambient conditions. (b) Red line: amplitude spectrum of the incident
 397 pump THz wave at the fundamental frequency $f = 0.3$ THz with the peak field strength $E_f = 85$
 398 kV/cm, determined in the reference measurement. Blue line: the spectrum of the same THz wave
 399 transmitted through graphene on a substrate, with clearly visible generated harmonics of 3rd, 5th
 400 and 7th order. (c) Pump wave (black line) and generated 3rd, 5th and 7th THz harmonics for the case
 401 in (b). The individual higher harmonics were Fourier filtered from the complete nonlinear signal
 402 containing all the generated harmonics at once. (d) Thermodynamic model calculation,
 403 corresponding to the measurements in (b,c), using the experimental fundamental pump wave at
 404 the frequency $f = 0.3$ THz (black line), and the basic parameters of graphene in full thermal
 405 equilibrium at 300 K as an input.

407 **Fig. 2** Illustration of the mechanism of THz harmonics generation in graphene, based on the
 408 calculations using the thermodynamic model of intraband nonlinear THz conductivity of graphene.
 409 (a) Temporal asymmetry of electron heating and cooling rates in graphene leads to a situation
 410 where the application of (b) a THz driving field to the graphene electron population results in (c)
 411 the electronic heat accumulation $\Delta Q(t)$ and hence in the temporal modulation of (d) the THz
 412 absorbance $A(t)$ and of the conductivity of graphene $\sigma(t)$. In these calculations the driving field (b)
 413 oscillates at the fundamental frequency $f = 0.3$ THz. Blue and red lines in (c,d) correspond to the
 414 driving field peak amplitude of 10 kV/cm and 85 kV/cm, respectively. The 10 kV/cm field strength
 415 represents the regime of small-signal nonlinearity (no significant modification of the sample
 416 properties on the timescale of the interaction with the THz wave), while the THz wave with 85
 417 kV/cm field strength leads to significant electron heating and thus to a substantial decrease in the
 418 absorption of graphene at the peak of interaction.

419 **Fig. 3.** THz high harmonics generation efficiency. (a) Dependency of the generated harmonic field
 420 strength on the fundamental pump field strength. For the third, fifth and seventh harmonic the
 421 fundamental field frequency was $f = 0.68$ THz, $f = 0.37$ THz, and $f = 0.3$ THz, respectively, leading to
 422 the corresponding higher harmonics of $3f = 2.04$ THz, $5f = 1.85$ THz, and $7f = 2.1$ THz, respectively.
 423 Symbols – data, black lines – parameter-free calculations using the thermodynamic model, dashed
 424 lines, power of 3 (red), power of 5 (green), and power of 7 (blue) fits corresponding to the small-
 425 signal nonlinearity regime below the driving field of ca. 20 kV/cm, which allows estimation of the

426 3rd, 5th and 7th order THz effective nonlinear susceptibilities of graphene $\chi^{(3)}_{\text{eff}}$, $\chi^{(5)}_{\text{eff}}$, and $\chi^{(7)}_{\text{eff}}$, as
427 indicated in the figure. The error bars for the pump fields are defined by the width of the chosen
428 pulse intensity distribution. The error bars for the harmonic fields are derived from the sum of the
429 standard deviations from multiple measurements and the background noise. (b) Calculation of
430 higher-order harmonic generation in graphene using the thermodynamic mechanism: amplitude
431 spectra of the THz field transmitted through the graphene sample. The calculation was performed
432 with sample parameters as used in this work ($N_c = 2.1 \times 10^{12} \text{ cm}^{-2}$ and $E_F = 170 \text{ meV}$), using the
433 model incident THz field at $f = 0.68 \text{ THz}$ with the peak strength in the range of 100 V/cm - 1
434 MV/cm. The harmonics up to the 13th order appear in the spectrum within the 10^6 dynamic range
435 with respect to the transmitted fundamental.

436

437

438

Methods

439 **Basic experimental setup.** The experiments were performed at the TELBE THz facility, which is providing
440 tunable, narrow-band (bandwidth of 20% (FWHM)), spectrally dense THz pulses in the frequency range
441 between 0.1 THz and 1.2 THz with adjustable repetition rates up to the few 100 kHz regime. The few
442 multicycle THz pulses are generated in an undulator through the process of superradiance from ultra-short
443 relativistic electron bunches accelerated and compressed in a quasi-CW superconducting radio frequency
444 accelerator [15].

445 In these specific experiments linearly polarized THz pulses with 0.3 THz, 0.37 THz, and 0.68 THz central
446 frequencies were employed separately as input fundamental driving field. The input THz beam was focused
447 onto the graphene sample at normal incidence and the transmitted (i.e. re-emitted) THz waves were
448 detected behind the sample (see Extended Data Fig. 1). All the measurements were carried out at room
449 temperature and under ambient atmosphere. The higher harmonic background was suppressed by
450 appropriate shaping of the longitudinal electron bunch form and by additional narrow bandpass filters [34]
451 before the sample, creating highly monochromatic pump fields with a bandwidth of roughly 10% (FWHM)
452 (Extended Data Fig. 2). Upon transmission through the sample, the THz signal containing the remainder of
453 the fundamental field, as well as the generated harmonics, was again sent through a set of band-pass filters
454 with the transmission band centered at the generated harmonic to be detected. The resulting THz field was
455 measured directly in the time-domain by free-space electro-optic sampling (FEOS) in a 1.9 mm thick ZnTe
456 crystal [35], with the peak THz field strength not exceeding ≈ 0.6 kV/cm. For FEOS THz detection, gating
457 pulses of 100 fs duration, central wavelength of 805 nm, from a commercial Ti:sapphire laser system [36]
458 were used, which is synchronized and timed to the TELBE source [15]. The uncertainty in the timing
459 between the THz pulses generated by the superradiant THz source and the probe laser pulses was less than
460 30 fs (FWHM) [37]. We note that the specific choice of the 1.9 mm thick ZnTe crystal enables sensitive THz
461 field sampling only in the frequency range below 2.5 THz, which in turn motivated our choice of the
462 fundamental frequencies of $f = 0.68$ THz, $f = 0.37$ THz, and $f = 0.3$ THz for the harmonics generation at $3f =$
463 2.04 THz, $5f = 1.85$ THz, and $7f = 2.1$ THz respectively.

464 To achieve the optimal dynamic range required for measuring the field dependence of these different
465 harmonics shown in Fig. 3(a) of the main text, specifically chosen bandpass filter combinations were used in
466 the individual experimental configurations which are described later in more detail. Combined with the
467 advanced pulse-resolved data acquisition scheme [37], a dynamic range of better than 10^3 in the time-
468 domain detection of seventh and third harmonic fields, and 10^9 in case of the fifth harmonic measurement
469 was achieved.

470 **Pulse-resolved determination of THz intensities and fields.** Depending on the tuning of the TELBE THz
471 source, intensities can fluctuate between 10% and 50% with respect to the average value. The intensity of
472 each THz pulse is recorded using a fast pyro detector with a bandwidth of 1 MHz in front of the first
473 bandpass filter (see Extended Data Fig. 1). The THz pulses are thereafter grouped and evaluated in separate
474 ranges around a certain pyro detector level. The width of these ranges defines the error bar in the pump
475 fields in Fig. 3(a) of the main text. The actual absolute values for the intensity and the corresponding THz
476 field are derived from a careful cross-calibration that has been carried out prior to the experiment. For this,
477 the intensity seen by the pyro detector was compared to that of the FEOS measurement at different pyro
478 detector levels. The THz intensity was dimmed in front of the pyro detector and in front of the ZnTe crystal

479 to avoid nonlinearities in both detection schemes. The resulting dependence between the THz intensities
480 obtained from the FEOS signal and the pyro detector level has subsequently been used to derive the THz
481 intensity/THz field for every single pulse. The peak fields at the sample position were determined from a
482 combination of the beam profile, as measured by a commercial pyroelectric camera [38], the THz pulse
483 shape, as measured by FEOS, and the THz power, as determined by a commercial calibrated THz power-
484 meter [39–41].

485 **Simultaneous detection of the third, fifth and seventh harmonic.** In this experiment, a fundamental
486 frequency of 0.3 THz was chosen for generation and detection of the seventh harmonic at 2.1 THz. The
487 repetition rate of the TELBE THz source was 100 kHz, the fs-laser had a corresponding rate of 200 kHz. The
488 particular configuration of bandpass filters, as shown in Extended Data Fig. 3, allowed not only the
489 detection of the 7th harmonic but also to simultaneously observe the 3rd and 5th harmonics at 0.9 THz and
490 1.5 THz (see Fig. 1 of the main text). Two 0.3 THz bandpass filters were used to suppress the harmonic
491 background of the undulator, leading to a maximum field strength of 85 kV/cm at the sample. The resulting
492 suppression factor in intensity is 10⁻⁸ for the 3rd, 10⁻⁶ for the 5th, and 10⁻⁴ for the 7th harmonic. The filtered
493 THz beam was focussed onto the sample, employing an off-axis parabolic mirror in combination with an
494 additional Teflon lens, which yielded a THz spot size of 560 μm (FWHM). A 2.1 THz bandpass filter was
495 utilized behind the sample to enable optimal sensitivity for the 7th harmonic in the EOS measurement,
496 while still allowing a detectable portion of the lower harmonics and the fundamental to pass through.

497 The as-measured HHG spectrum from graphene is shown in Extended Data Fig. 4 (red curve), clearly
498 showing the fundamental and harmonics up to the 7th order. The raw signal originating from the bare SiO₂
499 substrate as a reference is shown in black. To determine the corresponding electric fields quantitatively,
500 the transmission function of the 2.1 THz filter, as well as the frequency-dependent sensitivity of the ZnTe
501 detection crystal have to be included. The former has been measured and is displayed in the Extended Data
502 Fig. 4 as the grey curve, showing the substantial suppression of frequencies below 1.9 THz. We note that
503 the spectra presented in Fig. 1 (b) of the main text were obtained by deconvoluting the response functions
504 of both the ZnTe detection crystal and the 2.1 THz filter from the measured FEOS signals (see further
505 discussion in the next section of reconstructing the harmonic fields from the measured FEOS signals and
506 Extended Data Fig. 9). We also note that in order to not overly amplify the noise above 2.2 THz in the
507 graphene sample and reference spectra, the ZnTe sensitivity curve was assumed to be flat for values above
508 2.2 THz in this case. This does *not* affect either the overall peak shape in Fig. 1 of the main text, or the peak
509 field values that were used to calculate the HHG efficiencies (see Fig. 3(a) and Table 1 in the main text).

510 **Separate detection of the third and fifth harmonic at 2.04 THz and 1.85 THz.** The repetition rate of the
511 TELBE THz source was set to 101 kHz, the fs-laser used for FEOS detection had a repetition rate of 202 kHz.
512 To explicitly measure and quantify (cf. Fig. 3(a) of the main text) the signals from THG and FHG, we chose
513 the fundamental frequencies of 0.68 THz and 0.37 THz, respectively. Sets of narrow bandpass filters [34]
514 were tailored correspondingly. These filters suppress the higher harmonic background to less than 10⁻⁷ for
515 0.68 THz and to less than 10⁻¹¹ for 0.37 THz in intensity. Thereby, we reached an optimal dynamic range in
516 the FEOS detection of the harmonic field, despite the fact that the harmonic field is weaker than the
517 fundamental field by a factor of 10³ (THG) and 10⁻⁴ (FHG). Beam diameters (FWHM) on the sample surface
518 were 1 mm for 0.68 THz and 0.6 mm for 0.37 THz. In the latter case an additional Teflon lens was used to
519 optimize the spot size.

520 In Extended Data Fig. 5(a), we show a schematic of the beampath in the THG experiment. Here a single 1.93
521 THz bandpass filter [34] was introduced after the sample to attenuate the fundamental at 0.68 THz, while
522 allowing transmission of the THG signal at 2.04 THz. The spectral transmission function of the 1.93 THz filter
523 is shown in the Extended Data Fig. 6 (a). Extended Data Fig. 6(b) shows the as-measured amplitude spectra
524 of the detected FEOS signals: the reference (pump field transmitted through a bare SiO₂ substrate) and that
525 from the sample (pump field transmitted through graphene on a SiO₂ substrate). We note that the pump
526 field contains a small spurious contribution at the THG frequency (black line in Extended Data Fig. 6(b)),
527 which is, however, one order of magnitude smaller than the THG generated in graphene (red line in
528 Extended Data Fig. 6(b)).

529 In case of the THG experiment, the leaking intensity/field at the fundamental frequency $f = 0.68$ THz
530 measured through the bare SiO₂ substrate (geometry as shown in Extended Data Fig. 5(a)) serves as a
531 representative for the fundamental THz excitation field in Extended Data Fig. 10 and was used as a
532 reference input pulse in the theoretical model.

533 In the FHG experiment, we employed the beampath as schematically shown in Extended Data Fig. 5(b). To
534 ensure a larger sensitivity for the detection of the fifth harmonic field, the number of bandpass filters
535 before and after the sample was doubled for all fields except for the three highest field values shown in Fig.
536 3(a) for which the 0.4 THz filter was removed. Extended Data Fig. 7 shows the as-measured amplitude
537 spectra of the detected reference and sample FEOS signals. The transmission at the fundamental frequency
538 is strongly suppressed, while no spurious contribution of the pump field at the FHG frequency is observed.

539 Because of the overly small signal of the 0.37 THz fundamental in this configuration it was – in contrast to
540 the THG experiment – not suitable to derive the waveform of the fundamental THz pulse from the leaking
541 fundamental. Instead, the waveform was measured with an additional experimental configuration shown in
542 Extended Data Fig. 5(c). This waveform was also utilized as a reference input pulse for the theoretical
543 calculation of the nonlinear response of graphene.

544 **Reconstruction of the harmonic fields from the measured FEOS signals.** The complex-valued (i.e.
545 containing both amplitude and phase) field transmission functions of all optical elements in the THz
546 beampath of our experiments (sample substrate, bandpass filters), as well as the FEOS detector (THz
547 Fresnel insertion losses, and the frequency-dependent acceptance function of the FEOS ZnTe crystal which
548 is described in [42,43]) have been characterized, as summarized below. As a result, the rigorous
549 reconstruction of the measured FEOS signals back to the actual, calibrated THz electric field transients at all
550 frequencies of interest (fundamental, THG and FHG) was made possible. Our reconstruction from the FEOS
551 signals back to the actual fields follows the same general protocol reported in Ref. [44], while taking into
552 account all elements in the THz beampath. Here we exemplify the field reconstruction from the measured
553 EOS on the example of the THz THG experiment with $f = 0.68$ THz $\rightarrow 3f = 2.04$ THz.

554 Extended Data Fig. 6(a) shows the amplitude transmission spectrum of the 1.93 THz bandpass filter, while
555 Extended Data Fig. 8 below shows the phase and thereby time difference added to the signals at all
556 frequencies of interest due to the propagation through this optical element. A THz time-domain
557 spectroscopy measurement of the SiO₂ substrate yielded the values of frequency-dependent power
558 absorption coefficient of 7.6 cm⁻¹ (2.04 THz), 6.6 cm⁻¹ (1.85 THz), 2.3 cm⁻¹ (0.68 THz), and 1.3 cm⁻¹ (0.37
559 THz), and spectrally flat refractive index of 1.98, in good agreement with the literature [45].

560 In Extended Data Fig. 9(a), we show the frequency-dependent transmission response function (amplitude
561 transmission and phase shift) of the bare SiO_2 substrate, while in Extended Data Fig. 9(b) we show the
562 acceptance function (amplitude and phase shift) [42] of our FEOS unit: 1.9 mm thick ZnTe crystal, gated by
563 the 100 fs pulses at 805 nm central wavelength.

564 Taking all the above elements used in the THz transmission and detection in our experiment, we are now
565 able to rigorously reconstruct the as-measured THz FEOS signals back into the actual THz-field
566 waveforms [44], as shown in Extended Data Fig. 10 (example of THG measurement with $f = 0.68 \text{ THz} \rightarrow 3f$
567 = 2.04 THz).

568 Extended Data Fig. 10(a) shows the measured FEOS signals transmitted through the bare substrate (the
569 black pulse), through the graphene/substrate sample (the red pulse), both normalized to the peak of the
570 substrate pulse, and the difference between the two normalized FEOS signals (the blue pulse). The
571 difference pulse (the blue one) clearly shows oscillations at the THG frequency of 2.04 THz. Extended Data
572 Fig. 10(b) shows the corresponding reconstructed fields (the fields at the point just after the
573 graphene/substrate interface) after compensating for the field losses and deconvoluting the response
574 functions, described above, of the optical elements after the graphene/substrate interface. We note that
575 deconvoluting the phase shift induced by these optical elements after the graphene film from the FEOS
576 signals in Extended Data Fig. 10(a) results in a time-shift of $\sim 17.8 \text{ ps}$ to the reconstructed fields in Extended
577 Data Fig. 10(b). Further, in the reconstructed fields in Extended Data Fig. 10(b), the fundamental field is
578 upscaled to its original values before the bandpass filter attenuation after the sample, and in turn
579 dominates over the THG. Thus, the oscillation at the THG frequency included in the difference field pulse
580 (the blue pulse) in Extended Data Fig. 10(b), compared with that in Extended Data Fig. 10(a), is now less
581 pronounced. Now, if we spectrally remove the fundamental signal at 0.68 THz from the field difference
582 pulse shown in Extended Data Fig. 10(b), we arrive at the THG field waveform (Extended Data Fig. 10(c)).

583 **Sample preparation and characterization.** Our sample is a typical CVD-grown monolayer graphene
584 transferred onto a fused silica substrate [14,46,47]. The graphene quality was tested via Raman
585 spectroscopy that showed a single layer identity with a large-scale homogeneity (Extended Data Fig. 11(a)
586 for the Raman spectra of the sample). The characteristic graphene 2D and G peaks [48] are observed at
587 2703 cm^{-1} and 1591 cm^{-1} , respectively. The Gaussian shape of the 2D band with a FWHM of $\sim 47 \text{ cm}^{-1}$ along
588 with the relative ratio of the 2D peak to the G peak denotes single layer identity of the graphene sample.
589 The very weak D band at 1300 cm^{-1} is indicative of a low defect density.

590 The linear conductivity of our graphene sample was characterized via THz time-domain spectroscopy using
591 a ZnTe crystal as a THz emitter pumped by 800 nm laser pulses with a pulse width of 40 fs, and a repetition
592 rate of 1 kHz. The experimental data revealed Drude-type conductivity [14,49–52], providing the Fermi
593 level energy of 170 meV and electron momentum scattering time of 47 fs (see Extended Data Fig. 11(b) for
594 the linear THz characterization of the sample).

595 We note here that our graphene sample is, in fact, *p*-type, as is typical for the CVD-grown material
596 deposited onto fused SiO_2 substrate in the presence of ambient atmosphere (see e.g. [53]). However, due
597 to the symmetry of the band structure for Dirac electrons and holes in graphene, for simplicity, we depict
598 the Fermi level in the conduction rather than in the valence band.

599 **Calculations.** The (nonlinear) complex-valued THz field transmission from the free space through graphene
600 into the substrate is described by the Tinkham equation [54]

$$\tilde{E}_t(\omega) = \frac{2}{n_s + 1 + Z_0 \tilde{\sigma}(\omega)} \tilde{E}_{in}(\omega) \quad (\text{M1})$$

601 where n_s is the refractive index of the substrate, Z_0 is the free-space impedance and $\tilde{\sigma}(\omega)$ is the complex
 602 THz conductivity of the conductive film. The conductivity $\tilde{\sigma}(\omega)$ is nonlinear on the driving THz
 603 field [14,18,25,26,55,56], see also the discussion below.

604 The intraband conductivity of conduction band electrons of graphene at THz frequencies $\tilde{\sigma}(\omega)$ can
 605 generally be described by the solution of Boltzmann equation [3,14,57]:

$$\tilde{\sigma}(\omega) = -\frac{e^2 v_F}{2} \int_0^\infty D(E) \frac{\tau(E)}{1 - i\omega\tau(E)} \frac{\partial f_{FD}(E, \mu, T_e)}{\partial E} dE \quad (\text{M2})$$

606 where $v_F = 1 \times 10^6 m/s$ is the Fermi velocity of the relativistic Dirac-fermions in graphene, $\tau(E)$ is the
 607 carrier energy-dependent scattering time, $D(E) = 2|E|/\pi(\hbar v_F)^2$ is the density of states of the graphene
 608 energy bands, and $f_{FD}(E, \mu, T_e) = 1/[\exp(\frac{E-\mu}{k_B T_e}) + 1]$ is the Fermi-Dirac distribution function for a
 609 chemical potential μ and carrier temperature T_e .

610 The dominating electron momentum scattering mechanism in CVD-grown graphene deposited on fused
 611 silica substrate is the scattering via Coulomb interactions with charged impurities (long-range Coulomb
 612 scattering) [3,14,58–61], which is defined by linear dependence of scattering time on energy $\tau(E) = \gamma E$
 613 (see also [62]). The proportionality constant $\gamma = \tau_0/E_F = 47 \text{ fs}/170 \text{ meV}$ can be obtained from the linear
 614 response described above (see also [14] and Extended Data Fig. 11(b)). In terms of the THz induced heat
 615 density ΔQ , one can express $\tau(\Delta Q) = \gamma(E_F + \Delta Q/N_c)$, where $N_c = \int_0^\infty D(E)f_{FD}(E, \mu, T_e)dE$.

616 In order to compute the time-dependent THz field-induced heat ΔQ accumulated in the electronic system
 617 of graphene during the (nonlinear) interaction with the driving THz wave, the split-step time-domain
 618 calculations as common in nonlinear optics, must be performed (see e.g. [63]). For this, the inverse Fourier
 619 transforms of Eq. (M1) with the conductivity $\tilde{\sigma}(\omega)$ described by Eq. (M2) must be taken at every time step
 620 during numerical propagation. In order to speed up the calculations, a linear parameterization of the Eq.
 621 (M2) has been used, under the conditions of energy (all absorbed THz energy is adding to ΔQ) and free
 622 carrier density ($N_c = \int_0^\infty D(E)f_{FD}(E, \mu, T_e)dE = \text{const}$) conservation, yielding the following expression

$$\tilde{\sigma}(\omega) \approx \frac{(ev_F)^2 \tau_0 N_c / E_F}{1 - i\omega\tau(\Delta Q)} \quad (\text{M3})$$

623 Now, the time domain expression of the THz field transmission of graphene, by taking the inverse Fourier
 624 transform of Eq. (M1) with the conductivity $\tilde{\sigma}(\omega)$ described by Eq. (M3), results in a time-dependent
 625 response function

$$\mathcal{T}(t) = \left[\frac{2\delta(t)}{n_s + 1} - \frac{2Z_0(ev_F)^2 \gamma N_c}{(\tau_0 + \gamma\Delta Q(t)/N_c)(n_s + 1)^2} \exp\left\{-\frac{Z_0(ev_F)^2 \gamma N_c + n_s + 1}{(\tau_0 + \gamma\Delta Q(t)/N_c)(n_s + 1)} t\right\} \right] \quad (\text{M4})$$

626 where $\delta(t)$ is the Dirac delta. The convolution of this function with the temporal THz driving field $E_{in}(t)$
 627 yields the corresponding temporal field transmitted through the graphene film into the SiO_2 substrate

$$E_t(t) = \mathcal{T}(t) * E_{in}(t) \quad (\text{M5})$$

628 where $*$ -sign denotes the convolution.

629 In order to accommodate for the electron cooling due to phonon emission, we use the following cooling
 630 rate as directly measured in Ref. [20]

$$R(t) = 0.001 \exp\left(-\frac{t}{\tau_1}\right) + 0.46 \exp\left(-\frac{t}{\tau_2}\right) + 0.539 \exp\left(-\frac{t}{\tau_3}\right) \quad (\text{M6})$$

631 with time constants $\tau_1=13$ fs, $\tau_2=80$ fs and $\tau_3=0.86$ ps. This relaxation process leads to a recovery toward the
 632 initial linear conductivity of the graphene after the incident THz pulse ceases. The calculation of the THz
 633 induced heat is thus based on the following convolution:

$$\Delta Q(t) = \frac{1}{2} \varepsilon_0 c R(t) * \left[E_{inc}^2(t) - n_s E_t^2(t) - (E_t(t) - E_{inc}(t))^2 \right] \quad (\text{M7})$$

634 where ε_0 is the vacuum permittivity.

635 As a result, the time-dependent induced electronic heat given by Eq. (M7) leads to the temporal
 636 modulation of conductivity and results in the nonlinear response function of graphene described by Eq.
 637 (M4), which in turn leads to harmonics generation.

638 **The nonlinear THz refractive index of graphene.** The dielectric function of the graphene film can be
 639 expressed by [64,65]

$$\varepsilon_r = \varepsilon_\infty + \frac{i\tilde{\sigma}}{d\omega\varepsilon_0} \quad (\text{M8})$$

640 where $d = 0.3$ nm is the thickness of the graphene film and $\varepsilon_\infty \approx 1$ [64,65]. We calculate the real part of
 641 the refractive index using $n = \text{Re}\{\sqrt{\varepsilon_r}\}$. Substituting into Eq. (M8) for the conductivity by the linear Drude
 642 conductivity shown in Extended Data Fig. 11(b), we first obtained the linear (field-independent) refractive
 643 index (for fields less than 1 kV/cm). When the graphene film interacts with higher fields, the conductivity
 644 decreases as explained above, leading to a reduction in the refractive index [Extended Data Fig. 12]. In
 645 Extended Data Fig. 12(a), we show the calculated field-dependent THz index when the graphene film is
 646 pumped by THz fields at a fundamental frequency of 0.3 THz. In Extended Data Fig. 12(b), we show the THz
 647 field dependence of the nonlinear refractive index at the harmonics $3f = 2.04$ THz generated by $f = 0.68$ THz
 648 pump, $5f = 1.85$ THz generated by $f = 0.37$ THz pump, and $7f = 2.1$ THz generated by $f = 0.3$ THz pump. From
 649 this field dependence of the refractive index, we estimated the third, fifth and seventh order
 650 susceptibilities $\chi^{(3)}$, $\chi^{(5)}$ and $\chi^{(7)}$, respectively, as explained in the next section.

651 **Extraction of nonlinear coefficients of graphene.** The conservative, low-boundary estimate of the third,
 652 fifth and seventh-order THz nonlinear optical coefficients of graphene, based on the experimentally
 653 measured field conversion efficiencies in small-signal regime (power law fits to the data and the results of
 654 thermodynamic model in Fig. 3(a)) is done as follows. Ignoring both the pump field depletion (given $\sim 90\%$
 655 field transmission through graphene in the most absorptive limit of small driving THz fields), and the phase
 656 mismatch in $f \rightarrow mf$ conversion processes (negligible within one atomic layer), the conversion from the
 657 pump to the harmonic field is defined as $E_{mf} = \gamma L |E_f|^m$ with $\gamma = k_m \frac{\pi f}{cn_{mf}} \chi_{eff}^{(m)}$ [7,66]. Here $m = (3,5,7)$ is
 658 the harmonic order; E_f and E_{mf} are peak electric field strengths of the incident fundamental and generated
 659 m -th harmonic field, respectively; $k_m = (3/4, 5/16, 7/64)$ is a numerical coefficient for harmonics $m=3, 5$ and
 660 7 , respectively; $L = 0.3$ nm is the thickness of graphene layer [67]; c is the speed of light in vacuum; and n_{3f} ,
 661 n_{5f} and n_{7f} represent the refractive index of graphene at the harmonic frequencies, which at the target

662 harmonic frequency around 2 THz is chosen to be ~ 10 (see below) . From the measured 3rd harmonic
663 generation with $f = 0.68$ THz $\rightarrow 3f = 2.04$ THz, the field conversion coefficient of
664 $\gamma L = |E_{3f}|/|E_f|^3 = 1.79 \times 10^{-16} \text{ m}^2/\text{V}^2$, and an estimate of the effective third-order THz nonlinear
665 susceptibility of graphene is $\chi_{\text{eff}}^{(3)} \sim 1.7 \times 10^{-9} \text{ m}^2/\text{V}^2$. For the measured 5th harmonic generation with $f = 0.37$
666 THz $\rightarrow 5f = 1.85$ THz, the field conversion coefficient $\gamma L = |E_{5f}|/|E_f|^5 = 2.68 \times 10^{-30} \text{ m}^4/\text{V}^4$ and the
667 effective fifth-order THz nonlinear susceptibility of graphene is estimated as $\chi_{\text{eff}}^{(5)} \sim 1.2 \times 10^{-22} \text{ m}^4/\text{V}^4$. In the
668 same fashion, for the 7th harmonic generation process with $f = 0.3$ THz $\rightarrow 7f = 2.1$ THz, the field conversion
669 coefficient $\gamma L = |E_{7f}|/|E_f|^7 = 1.8 \times 10^{-46} \text{ m}^6/\text{V}^6$ and the estimate of the effective seventh-order THz
670 nonlinear susceptibility of graphene is $\chi_{\text{eff}}^{(7)} \sim 1.74 \times 10^{-38} \text{ m}^6/\text{V}^6$.

671 We note that the value for the refractive index of graphene of $n_{3f,5f,7f} \sim 10$ (at the frequency around 2 THz,
672 and at high electron temperature) used in our calculations is a conservative order-of-magnitude estimate,
673 as the actual values can be as high as $n \sim 20-80$ (Extended Data Fig. 12(b)), which will increase the values of
674 the retrieved nonlinear coefficients of graphene even further.

675 **Limits of the thermodynamic model of THz response of graphene in terms of driving THz field strength.**

676 The electron response, following the heating-cooling dynamics of electron population as described in this
677 paper, will dominate the THz intraband nonlinearity of graphene until the regime of coherent Bloch
678 oscillations will be reached. In this regime (see e.g. [13,68]), the conduction band electron reaches the
679 Brillouin zone boundary in the time faster than the typical electron momentum scattering (Drude) time,
680 providing for the coherent nonlinear current (Bloch) oscillations in the k space of the Brillouin zone
681 between the $k = \pi/a$ and $-k = -\pi/a$ points, where a is the lattice constant. We use the acceleration theorem
682 $\frac{dk}{dt} = -eE/\hbar$ which can be further simplified to $\frac{\Delta k}{\tau} = -eE/\hbar$, where $\Delta k = \pi/a$ is the Brillouin zone half-width,
683 a = 0.14 nm is the lattice constant of graphene, and τ is the electron momentum relaxation time. For the
684 typical electron momentum relaxation time in the range $\tau = 10-100$ fs (see e.g. [3]) we arrive at the electric
685 field strength range $E = 1 - 10$ MV/cm. This field strength thus sets the estimated upper validity limit for our
686 model.

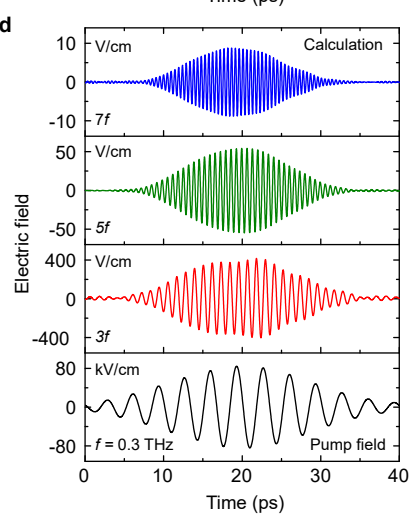
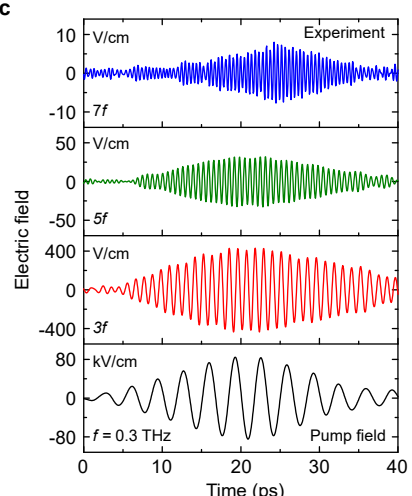
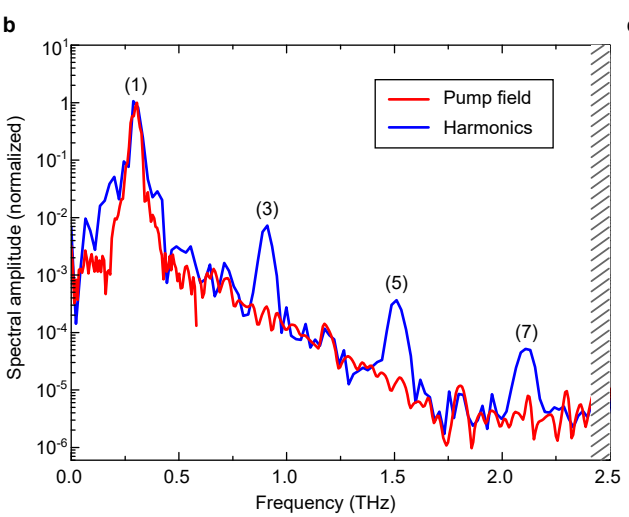
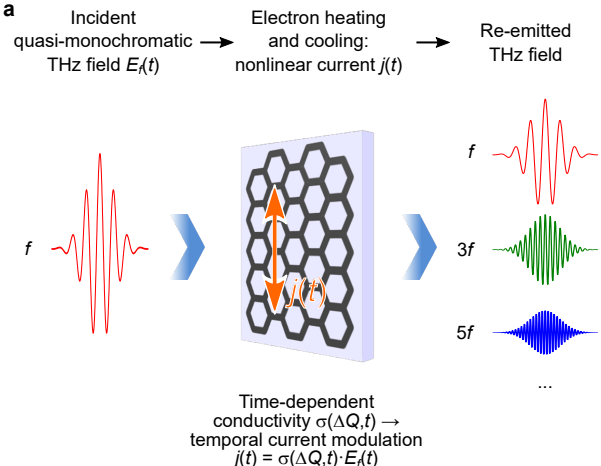
687

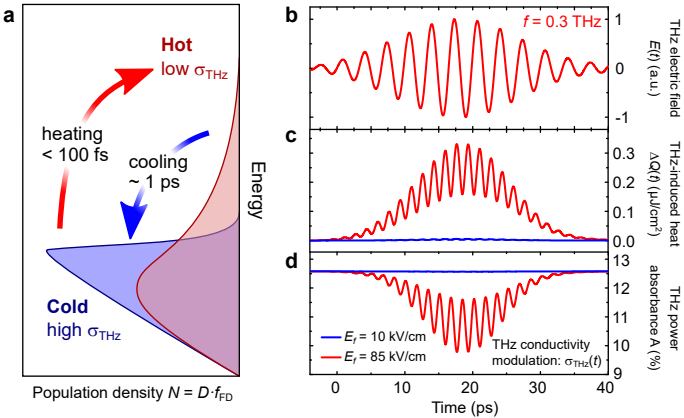
688 **References / Methods**

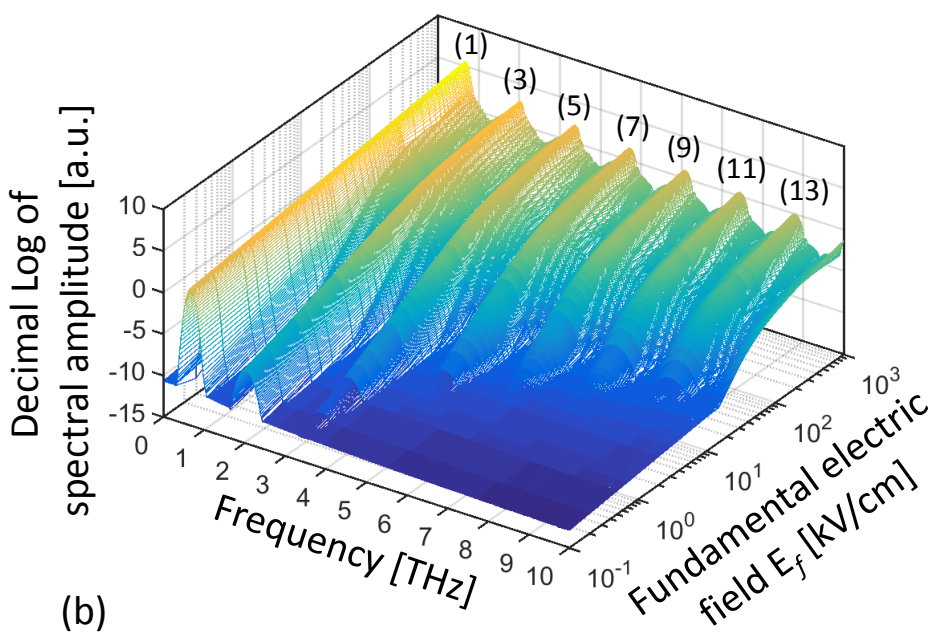
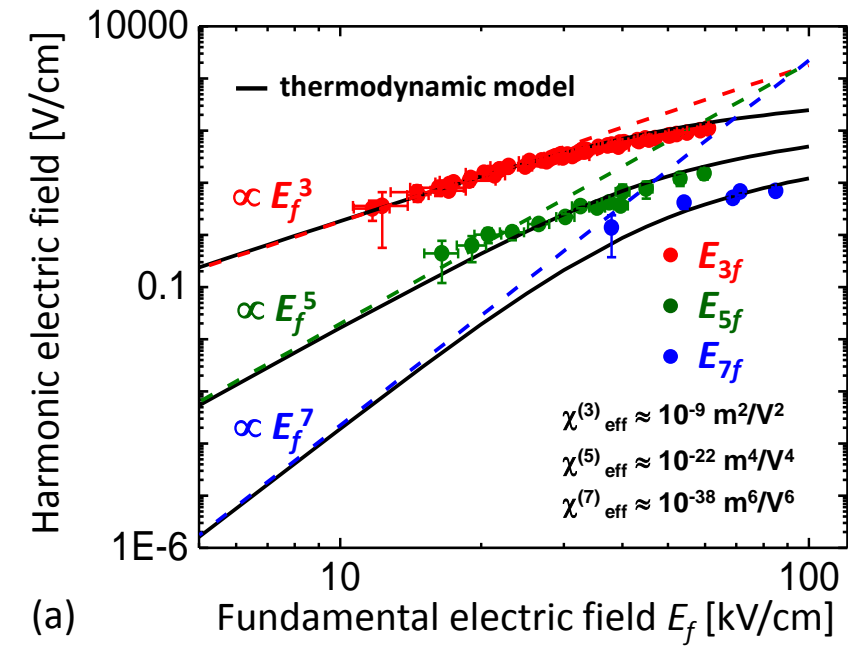
- 689 34. S. A. Kuznetsov, M. A. Astafyev, A. V Gelfand, and A. V Arzhannikov, "Microstructured
690 frequency selective quasi-optical components for submillimeter-wave applications," in
691 44th European Micorwave Conference (EuMC) (2014), p. 881.
- 692 35. Q. Wu, M. Litz, and X. C. Zhang, "Broadband detection capability of ZnTe electro-optic
693 field detectors," Appl. Phys. Lett. **68**, 2924–2926 (1996).
- 694 36. <https://cohrcdn.azureedge.net/assets/pdf/RegA-Data-Sheet.pdf>
- 695 37. S. Kovalev, B. Green, T. Golz, S. Maehrlein, N. Stojanovic, A. S. Fisher, T. Kampfrath, and M.
696 Gensch, "Probing ultra-fast processes with high dynamic range at 4th-generation light
697 sources: Arrival time and intensity binning at unprecedented repetition rates," Struct.
698 Dyn. **4**, 24301 (2017).
- 699 38. [www.ophiropt.com/laser--measurement/beamprofilers/products/Beam-
700 Profiling/Camera-Profiling-with-BeamGage/Pyrocam-IIIHR](http://www.ophiropt.com/laser--measurement/beamprofilers/products/Beam-Profiling/Camera-Profiling-with-BeamGage/Pyrocam-IIIHR).

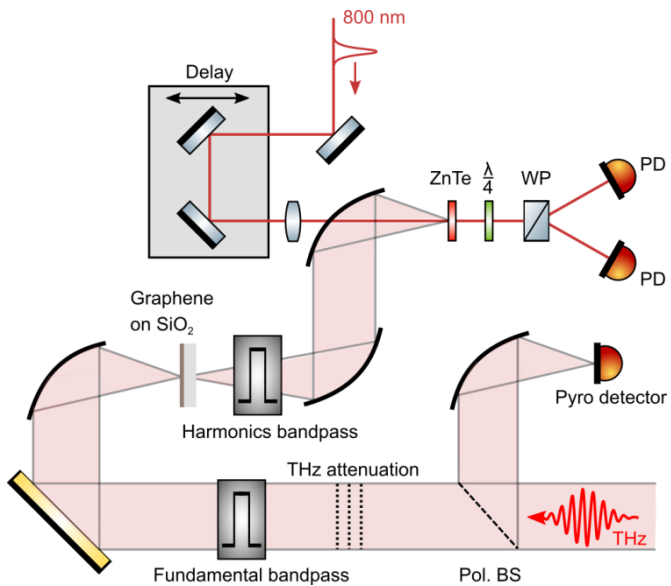
- 701 39. www.ophiropt.com/laser--measurement/laser-power-energy-meters/products/Laser-
702 [Thermal-Power-Sensors/High-Sensitivity-Thermal-Laser-Sensors/3A-P-THz](#).
- 703 40. A. Steiger, M. Kehrt, C. Monte, and R. Müller, "Traceable terahertz power measurement
704 from 1 THz to 5 THz," *Opt. Express* **21**, 14466 (2013).
- 705 41. R. Müller, W. Bohmeyer, M. Kehrt, K. Lange, C. Monte, and A. Steiger, "Novel detectors for
706 traceable THz power measurements," *J. Infrared, Millimeter, Terahertz Waves* **35**, 659–
707 670 (2014).
- 708 42. G. Gallot, J. Zhang, R. W. McGowan, T. Jeon, and D. Grischkowsky, "Measurements of the
709 THz absorption and dispersion of ZnTe and their relevance to the electro-optic detection
710 of THz radiation," *Appl. Phys. Lett.* **74**, 3450 (1999).
- 711 43. Q. Wu and X. Zhang, "Ultrafast electro-optic field sensors," *Appl. Phys. Lett.* **68**, 1604
712 (1996).
- 713 44. T. Kampfrath, M. Battiato, P. Maldonado, G. Eilers, J. Nötzold, S. Mährlein, V. Zbarsky, F.
714 Freimuth, Y. Mokrousov, S. Blügel, M. Wolf, I. Radu, P. M. Oppeneer, and M. Münzenberg,
715 "Terahertz spin current pulses controlled by magnetic heterostructures," *Nat. Nanotechnol.* **8**,
716 256–260 (2013).
- 717 45. T. J. Parker and J. E. Ford, "The optical constants of pure far-infrared," *Infrared Phys.* **18**,
718 215–219 (1978).
- 719 46. X. Li, W. Cai, J. An, S. Kim, J. Nah, D. Yang, R. Piner, A. Velamakanni, I. Jung, E. Tutuc, S. K.
720 Banerjee, L. Colombo, and R. S. Ruoff, "Large-area synthesis of high-quality and uniform
721 graphene films on copper foils," *Science* **324**, 1312–1314 (2009).
- 722 47. Y. Hao, M. S. Bharathi, L. Wang, Y. Liu, H. Chen, S. Nie, X. Wang, H. Chou, C. Tan, B.
723 Fallahazad, H. Ramanarayanan, C. W. Magnuson, E. Tutuc, B. I. Yakobson, K. F. McCarty, Y.
724 Zhang, P. Kim, J. Hone, L. Colombo, and R. S. Ruoff, "The role of surface oxygen in the
725 growth of large single-crystal graphene on copper," *Science* **342**, 720–723 (2013).
- 726 48. A. C. Ferrari, J. C. Meyer, V. Scardaci, C. Casiraghi, M. Lazzeri, F. Mauri, S. Piscanec, D.
727 Jiang, K. S. Novoselov, S. Roth, and A. K. Geim, "Raman spectrum of graphene and
728 graphene layers," *Phys. Rev. Lett.* **97**, 187401 (2006).
- 729 49. K. F. Mak, L. Ju, F. Wang, and T. F. Heinz, "Optical spectroscopy of graphene: From the far
730 infrared to the ultraviolet," *Solid State Commun.* **152**, 1341–1349 (2012).
- 731 50. G. Jnawali, Y. Rao, H. Yan, and T. F. Heinz, "Observation of a transient decrease in
732 terahertz conductivity of single-layer graphene induced by ultrafast optical excitation,"
733 *Nano Lett.* **13**, 524–530 (2013).
- 734 51. J. M. Dawlaty, S. Shivaraman, J. Strait, P. George, M. Chandrashekhar, Y. Chen, F. Rana, M.
735 G. Spencer, D. Veksler, and Y. Chen, "Measurement of the optical absorption spectra of
736 epitaxial graphene from terahertz to visible," *Appl. Phys. Lett.* **93**, 131905 (2008).
- 737 52. A. J. Frenzel, C. H. Lui, W. Fang, N. L. Nair, P. K. Herring, P. Jarillo-Herrero, J. Kong, and N.
738 Gedik, "Observation of suppressed terahertz absorption in photoexcited graphene,"
739 *Appl. Phys. Lett.* **102**, 113111 (2013).
- 740 53. H. I. Wang, M.-L. Braatz, N. Richter, K.-J. Tielrooij, Z. Mics, H. Lu, N.-E. Weber, K. Müllen, D.
741 Turchinovich, M. Kläui, and M. Bonn, "Reversible photochemical control of doping levels
742 in supported graphene," *J. Phys. Chem. C* **121**, 4083–4091 (2017).

- 743 54. R. E. Glover and M. Tinkham, "Conductivity of superconducting films for photon energies
744 between 0.3 and 40kT_c," Phys. Rev. **108**, 243–256 (1957).
- 745 55. R. J. Suess, S. Winnerl, H. Schneider, M. Helm, C. Berger, W. A. de Heer, T. E. Murphy, and
746 M. Mittendorff, "Role of Transient Reflection in Graphene Nonlinear Infrared Optics,"
747 ACS Photonics **3**, 1069–1075 (2016).
- 748 56. H. A. Hafez, P. L. Lévesque, I. Al-Naib, M. M. Dignam, X. Chai, S. Choubak, P. Desjardins, R.
749 Martel, and T. Ozaki, "Intense terahertz field effects on photoexcited carrier dynamics in
750 gated graphene," Appl. Phys. Lett. **107**, 251903 (2015).
- 751 57. M. P. Marder, "Transport phenomena and Fermi liquid theory," in Condensed Matter
752 Physics (John Wiley & Sons, Inc., 2010), pp. 483–493.
- 753 58. K. J. Tielrooij, J. C. W. Song, S. A. Jensen, A. Centeno, A. Pesquera, A. Zurutuza Elorza, M.
754 Bonn, L. S. Levitov, and F. H. L. Koppens, "Photoexcitation cascade and multiple hot-
755 carrier generation in graphene," Nat. Phys. **9**, 248–252 (2013).
- 756 59. E. H. Hwang and S. Das Sarma, "Acoustic phonon scattering limited carrier mobility in
757 two-dimensional extrinsic graphene," Phys. Rev. B **77**, 115449 (2008).
- 758 60. E. H. Hwang and S. Das Sarma, "Screening-induced temperature-dependent transport in
759 two-dimensional graphene," Phys. Rev. B **79**, 165404 (2009).
- 760 61. V. Perebeinos and P. Avouris, "Inelastic scattering and current saturation in graphene,"
761 Phys. Rev. B **81**, 195442 (2010).
- 762 62. M. Lundstrom, Fundamentals of Carrier Transport (Cambridge University Press, 2000).
- 763 63. X. Liu, J. Laegsgaard, and D. Turchinovich, "Self-stabilization of a mode-locked
764 femtosecond fiber laser using a photonic bandgap fiber," Opt. Lett. **35**, 913–915 (2010).
- 765 64. I. Lin, J. Liu, K. Shi, P. Tseng, K. Wu, C. Luo, and L. Li, "Terahertz optical properties of
766 multilayer graphene : Experimental observation of strong dependence on stacking
767 arrangements and misorientation angles," Phys. Rev. B **86**, 235446 (2012).
- 768 65. J. Gosciniak and D. T. H. Tan, "Theoretical investigation of graphene-based photonic
769 modulators," Sci. Rep. **3**, 1897 (2013).
- 770 66. S. M. Saltiel, A. A. Sukhorukov, and Y. S. Kivshar, "Multistep Parametric Processes in
771 Nonlinear Optics," in Progress in Optics, E. Wolf, ed., 47th ed. (Elsevier, 2005).
- 772 67. C. J. Shearer, A. D. Slattery, A. J. Stapleton, J. G. Shapter, and C. T. Gibson, "Accurate
773 thickness measurement of graphene," Nanotechnology **27**, 125704 (2016).
- 774 68. M. Hohenleutner, F. Langer, O. Schubert, M. Knorr, U. Huttner, S. W. Koch, M. Kira, and R.
775 Huber, "Real-time observation of interfering crystal electrons in high-harmonic
776 generation," Nature **523**, 572–575 (2015).
- 777
- 778

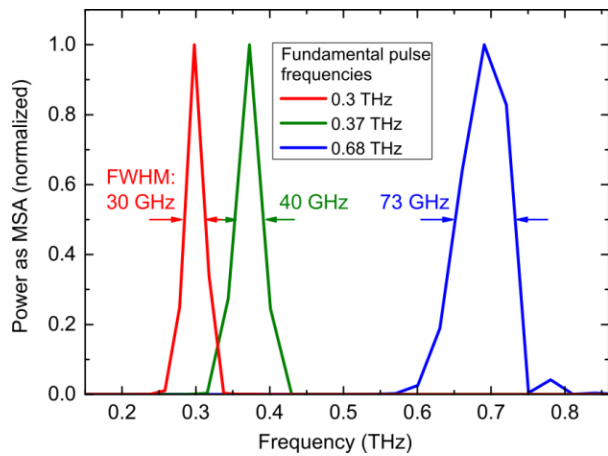




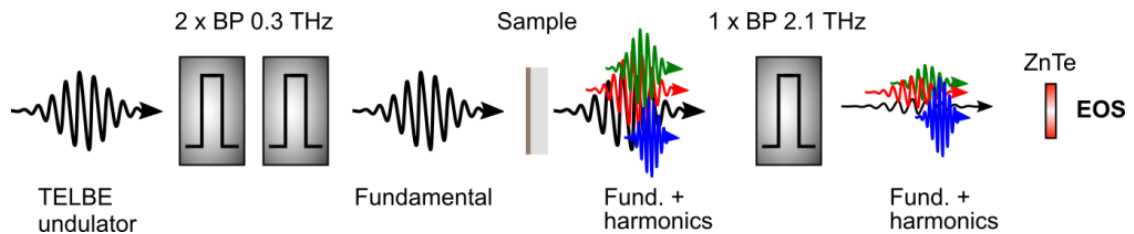




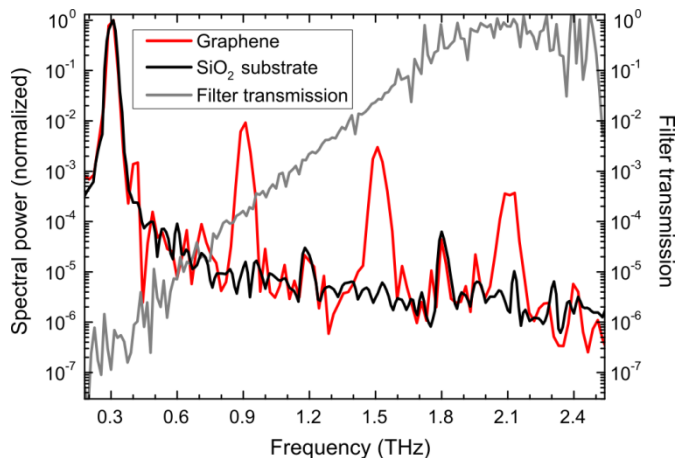
Extended Data Fig. 1: Experimental set-up. Tunable multicycle THz pulses (red) from the undulator of the TELBE facility² are used to irradiate the graphene sample. 100-fs pulses from a Ti:sapphire laser system (brown) are used to probe the transmitted and emitted THz pulses by free-space electro-optic sampling. PD, photodiode; BS, beamsplitter; Pol., polarizer.



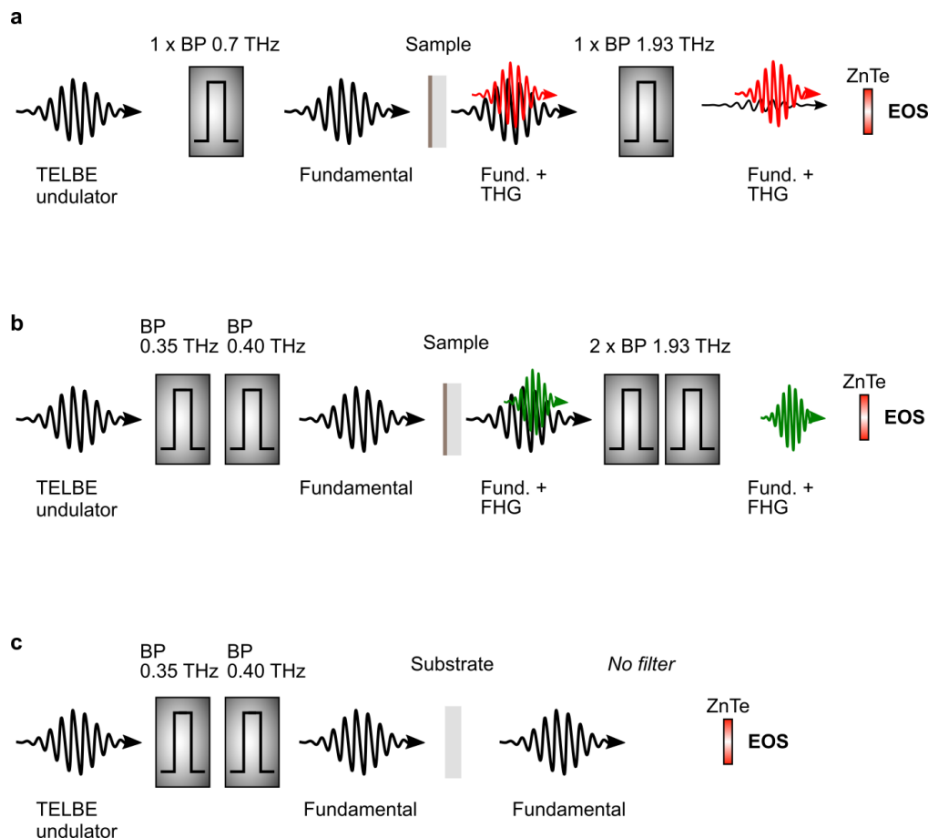
Extended Data Fig. 2: Fundamental frequencies after bandpass filtering. The bandwidths were determined from Gaussian fits to the spectra. MSA, mean square amplitude.



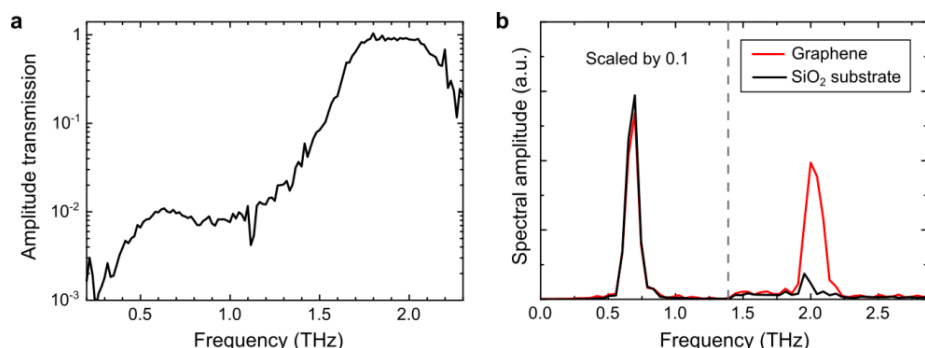
Extended Data Fig. 3: Scheme of the set-up for detection of multiple harmonics up to the seventh order. Two 0.3-THz bandpass filters (BP) are used to suppress the undulator harmonic background. A single 2.1-THz bandpass filter after the sample attenuates the fundamental, third and fifth harmonics to an extent that they can still be detected by the EOS set-up.



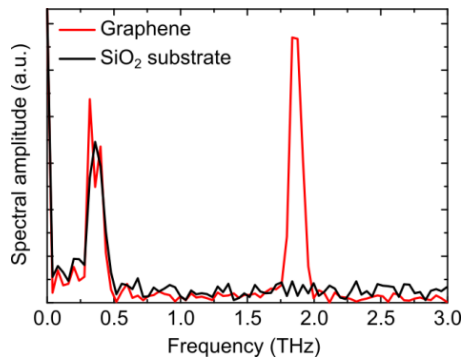
Extended Data Fig. 4: HHG signal from graphene, reference signal from the SiO_2 substrate and filter function of the 2.1-THz bandpass.
The red curve shows the as-measured HHG spectrum of the graphene sample. The black curve shows the reference spectrum taken from the bare SiO_2 substrate. The measured transmission function of the 2.1-THz bandpass filter is also shown (grey line).



Extended Data Fig. 5: Schemes of the experimental configurations to determine the electric fields of the fundamental, THG and FHG pulses. Measurements were performed with graphene/SiO₂ and with the bare SiO₂ substrate. **a**, Set-up for the THG experiment used to measure the fundamental and harmonic simultaneously. **b**, Set-up to measure the harmonic in the FHG experiment. Two filters were used before the sample and two after the sample, to optimize the signal-to-noise ratio. **c**, Set-up to determine the electric fields for the fundamental in the FHG experiment.

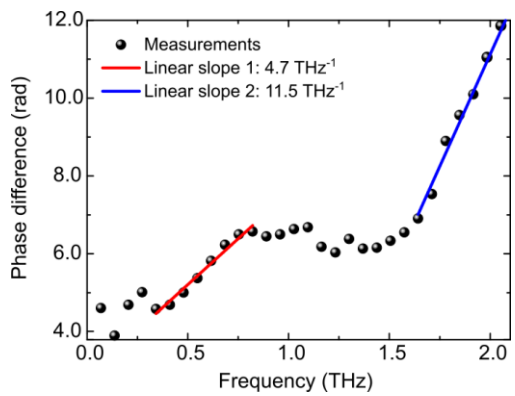


Extended Data Fig. 6: Filter function of the 1.93-THz bandpass and raw spectra from the THG experiment. **a**, Amplitude transmission function of a single 1.93-THz bandpass filter. **b**, As-measured spectral amplitude in arbitrary units (a.u.), as determined from the bare SiO₂ substrate (black) and from the graphene sample (red). The incident THz peak field of the fundamental at 0.68 THz was 61 kV cm⁻¹.

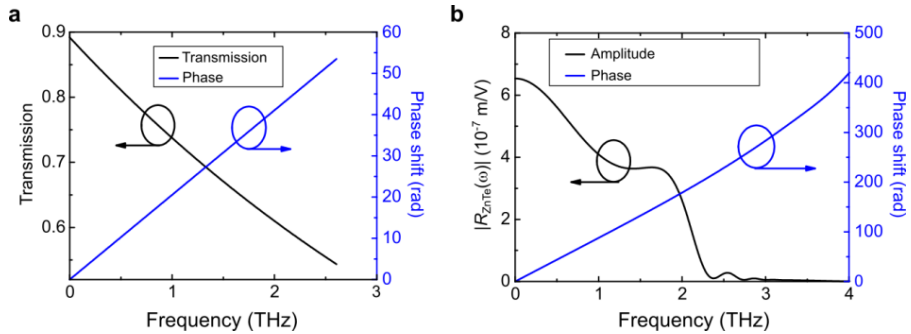


Extended Data Fig. 7: Raw spectra from the FHG experiment.

These as-measured spectra show the spectral amplitude as determined from a measurement with the bare SiO₂ substrate as a reference and a measurement of the graphene sample. The incident THz peak field in the fundamental at 0.37 THz was 40 kV cm⁻¹ when using two filters in the incident beam. Insignificant transmission at the fundamental frequency and no spurious background at the FHG frequency band is observed in the reference field measurement.

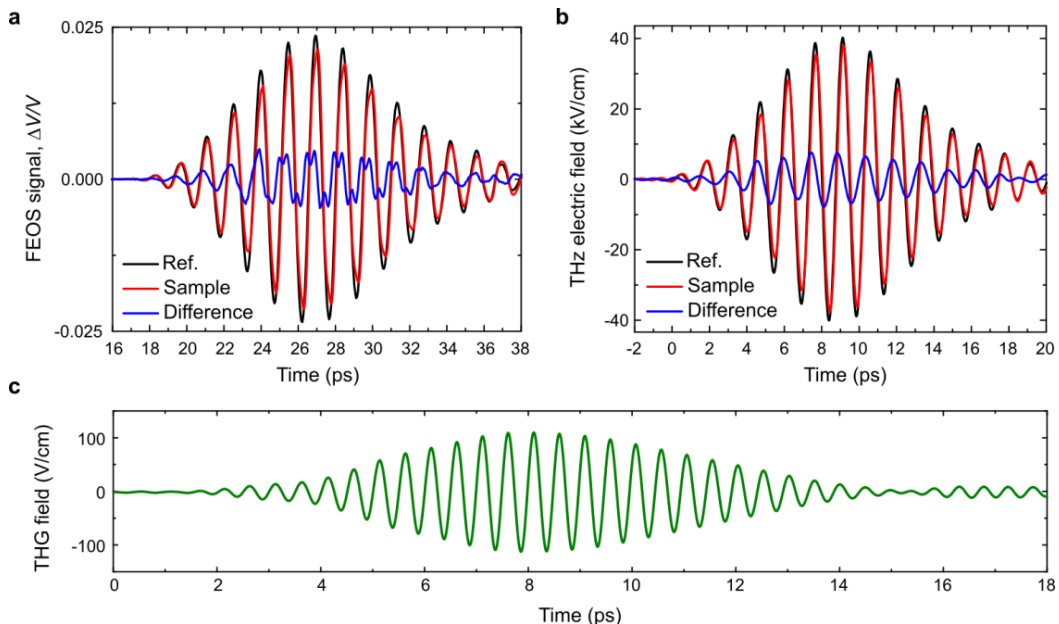


Extended Data Fig. 8: Frequency-dependent phase difference induced by the 1.93-THz bandpass filter.

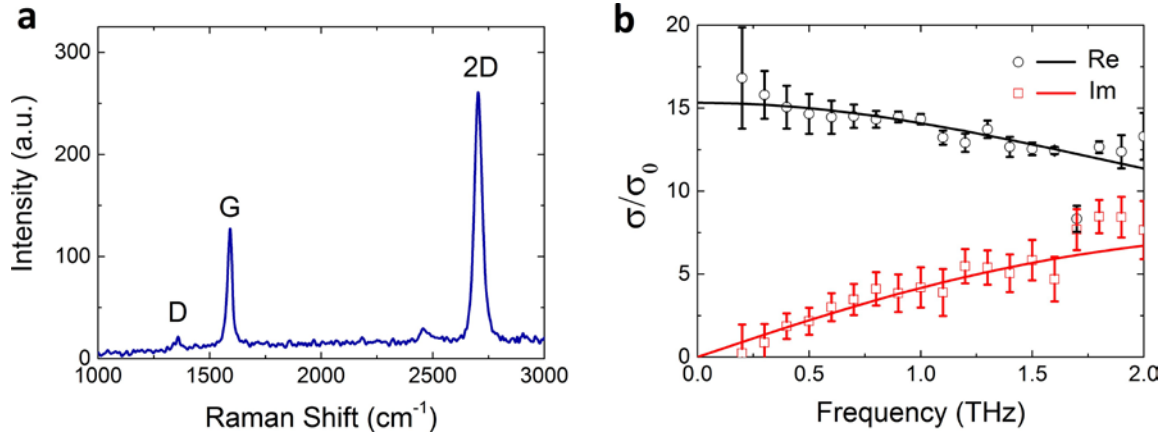


Extended Data Fig. 9: The frequency-dependent response function.

a, The bare substrate described by the amplitude transmission (black line) and the substrate-induced phase shift (blue line).
b, A simulated acceptance function of the 1.9-mm-thick ZnTe detection crystal; amplitude (black curve) and phase shift (blue curve). Arrows indicate relevant axis.

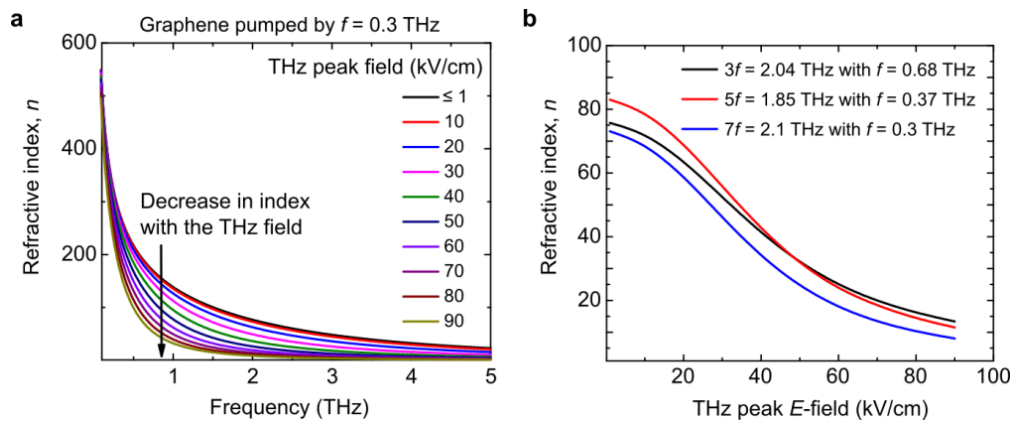


Extended Data Fig. 10: Reconstruction of the harmonic fields from the measured FEOS signals. This is an example of THG measurement with $f = 0.68 \text{ THz} \rightarrow 3f = 2.04 \text{ THz}$. **a**, Measured FEOS signals (dimensionless). **b**, The corresponding fields transmitted through the incidence interface of the sample after deconvoluting the response functions of all the elements after the graphene film, including the 1.9-mm-thick ZnTe detection crystal, the 1.93-THz filter and the fused silica substrate from the FEOS signals in **a**. Black pulse is for the bare substrate, red for the graphene sample and blue for the difference. **c**, The pure THG field extracted from the blue field pulse in **b**.



Extended Data Fig. 11: Characterization of the graphene sample.

a, Raman spectrum of the graphene sample. **b**, Linear conductivity, real and imaginary, of the graphene film normalized to the universal conductivity $\sigma_0 = e^2/(4\hbar)$. The symbols represent the experimental data; the solid lines represent the Drude fit with a Fermi level energy $EF = 170$ meV (corresponding to a doping concentration $N_c = 2.1 \times 10^{12}$ cm $^{-2}$) and a scattering time $\tau_0 = 47$ fs as fitting parameters. The error bars are the standard deviation in the measurements.



Extended Data Fig. 12: The nonlinear (THz-field-dependent) refractive index of the graphene film. **a**, The THz refractive index of the graphene film as a function of frequency at various peak electric fields for the THz pump at 0.3 THz, showing reduction in the refractive index with both frequency and exciting field strength. **b**, The field dependence of the nonlinear THz refractive index at the harmonics $3f = 2.04$ THz generated by $1f = 0.68$ THz pump, $5f = 1.85$ THz generated by $1f = 0.37$ THz pump, and $7f = 2.1$ THz generated by $1f = 0.3$ THz pump.